REPORT DOCUMENTATION PAGE

Form Approved
OMB NO. 0704-0188

1. AGENCY USE ONLY (Leave Blank)	2. REPORT DATE 31 Mar 2004	3. REPORT TYPE AND DATES COVERED Final Report 01 Oct 00 – 31 Dec 03

4. TITLE AND SUBTITLE
Mitigation of Atmospheric Effects on Imaging Systems

5. FUNDING NUMBERS
C: DAAD19-00-1-0503

6. AUTHOR(S)
Gary G. Gimmestad, Mikhail S. Belen'kii

7. PERFORMING ORGANIZATION NAME(S) AND ADDRESS(ES)
Georgia Tech Research Institute, 400 W. 10th Street, Atlanta, GA 30332
Trex Enterprises, 10455 Pacific Center Court, San Diego, CA 92121

8. PERFORMING ORGANIZATION REPORT NUMBER

9. SPONSORING / MONITORING AGENCY NAME(S) AND ADDRESS(ES)

U. S. Army Research Office
P.O. Box 12211
Research Triangle Park, NC 27709-2211

10. SPONSORING / MONITORING AGENCY REPORT NUMBER

40432.1-CI

11. SUPPLEMENTARY NOTES
The views, opinions and/or findings contained in this report are those of the author(s) and should not be construed as an official Department of the Army position, policy or decision, unless so designated by other documentation.

12 a. DISTRIBUTION / AVAILABILITY STATEMENT	12 b. DISTRIBUTION CODE
Approved for public release; distribution unlimited.	

13. ABSTRACT (Maximum 200 words)

Atmospheric effects such as refractive turbulence and aerosol obscuration can seriously degrade the performance of military optical systems. A complete understanding of these effects is therefore essential for optimizing the design of such systems, and it is also necessary for developing mitigation techniques. The project described here was a three-year theoretical and experimental investigation to develop and validate a physical understanding of several atmospheric effects that are important for current and future Army optical systems.

a) An investigation of turbulence-induced waviness in images of edges, and techniques for its mitigation.

b) An investigation of the degradation of optical images by atmospheric turbulence and a validation of the predicted dependence of the atmospheric Modulation Transfer Function (MTF) on the inner scale of turbulence.

14. SUBJECT TERMS
tilt anisoplanatism, pointing error, edge waviness, statistical analysis, image processing, mitigation technique, mtf, turbulence

15. NUMBER OF PAGES
24

16. PRICE CODE

17. SECURITY CLASSIFICATION OR REPORT	18. SECURITY CLASSIFICATION ON THIS PAGE	19. SECURITY CLASSIFICATION OF ABSTRACT	20. LIMITATION OF ABSTRACT
UNCLASSIFIED	UNCLASSIFIED	UNCLASSIFIED	UL

NSN 7540-01-280-5500

Standard Form 298 (Rev.2-89)
Prescribed by ANSI Std. 239-18
298-102

Foreword

This report describes a three-year experimental study of atmospheric effects on imaging systems. The test scenarios were all ground-to-ground using both visible and infrared wavelengths, in order to have the most relevance to the surveillance and combat scenarios encountered by the US Army. Image degradation effects caused by refractive turbulence and aerosol extinction are both at their worst near the ground, and mitigation techniques to improve image quality were addressed in the study where possible. Three sets of field tests were performed, all on airport runways in Atlanta, Georgia. Two of the studies addressed waviness in images through the turbulent atmosphere by recording images of specially designed targets, while the third study addressed the atmospheric modulation transfer function (MTF) through analysis of images of point sources. The project was a collaborative effort involving the Georgia Tech Research Institute, Trex Enterprises, and the Army Research Laboratory.

Table of Contents

List of Illustrations

Statement of Problem Studied

Atmospheric effects including refractive turbulence and aerosol obscuration can seriously degrade the performance of both optical imaging and laser systems for military applications. These atmospheric degradation effects are the most severe near the ground, where both the strength of turbulence and the aerosol concentration are the highest. A complete understanding of these degradation effects is therefore essential for performance analysis, reliable system design, and development of efficient mitigation techniques.

Image degradation was addressed experimentally in two ways: by recording images of specially designed large-area targets through the turbulent atmosphere, and by recording images of point sources. The large-area images were analyzed to find wave front tilt correlations, while the point source images were analyzed to find the atmospheric modulation transfer function (MTF). In both cases, images were recorded in both visible and infrared (IR) spectral regions.

Results Summary
I. Purpose 1: Characterization and Mitigation of Image Edge Waviness

Motivation
The most common degradation effect of turbulence on imaging system is edge waviness. When an extended object is imaged through the turbulent atmosphere, edges in the image appear wavy.[1-3] The latter effect occurs due to the fact that light waves emitted from different portions of the object propagate through different atmospheric paths and traverse different turbulent inhomogeneities. Consequently, these light waves acquire different atmospheric tilts. This phenomenon is commonly referred to as tilt anisoplanatism.[4] Edge image waviness caused by tilt anisoplanatism reduces the accuracy of target localization and optical tracking, and it makes target identification and verification of target identity more difficult.

A similar degradation effect occurs in laser weapon systems such as the Airborne Laser (ABL)[5] and the tactical high energy laser (HEL) system.[6] In this application, when a track point and an aim point at the target are separated by some angular distance, a track beam and a HEL weapon beam will propagate in slightly different directions and acquire different tilts. The different tilts result in a pointing error.

Finally, the same degradation effect occurs in laser power beaming[7] and active satellite imaging systems.[8] In these cases, in order to compensate for the round-trip time of flight associated with the finite speed of light and satellite motion, the laser beam is pointed at a point-ahead angle. Since the optical tracker and the transmitted beam are pointed in different directions, a residual pointing error caused by tilt anisoplanatism occurs. Because tilt anisoplanatism limits performance of many practical systems, a detailed understanding of this phenomenon, as well as mitigation techniques to correct for it, are important.

These considerations motivated the research team to perform a detailed experimental study of tilt anisoplanatism for ground-to-ground scenarios. This study included the development of a specialized dual-waveband optical imaging system, field tests, data analysis and interpretation.

Optical Sensors and Experiment

To make simultaneous measurements of atmospheric tilt in two spectral wavebands, a dual-band imaging system was built. The system was based on a 40-cm Newtonian telescope with a 1.8 m focal length. The imaging system had two cameras: an Electrim camera sensitive in the visible ($0.6\,\mu$m) waveband and an Amber QWIP infrared camera sensitive in the 9–micron region.

The Amber QWIP infrared camera had 256x256 pixels, pixel pitch 38 μm, focal length of 1.8 m, FOV of 5.4 x5.4 mr, and pixel FOV 21.1 μrad. This camera was mounted with its focal plane array in the telescope's focal plane. The Electrim camera had 242x324 pixels, pixel pitch 10 μm, focal length 0.8 m, total FOV of 3x4 mr. and pixel FOV 12.5 μrad. A Germanium beamsplitter was placed at a 45-degree angle in the converging light cone to act as a dichroic mirror, reflecting visible light to the Electrim camera through relay optics that gave the visible-light camera the same field of view (FOV) as the infrared camera. A rotating mask was mounted on the front of the telescope to give selectable apertures of 6, 9, and 12 *cm* diameter. The apertures were off center so as to use an unobstructed light path. By removing the mask it was possible to use the full 40 *cm* telescope aperture.

The Amber camera had a fixed frame rate of 60 frames per second. Digital data is available at this frame rate, and standard RS-170 video data is also always available. A dedicated PC computer with a frame grabber was interfaced to the Amber to record its digital data, and a VHS videocassette recorder (VCR) was used to record the video signal.

A second dedicated PC computer was interfaced to the Electrim camera to record digital imagery in the visible-light region. The visible system was capable of recording at higher frame rates, but it was used at 60 frames per second to match the infrared camera. The Electrim camera does not provide a video signal. In order to obtain visible-light video for direct comparison with the infrared video, a JVC black and white camera was used in place of the Electrim and its output was recorded with a second VHS VCR.

The wave front tilt was measured in two different ways. In the first case we used an array of small discrete sources. For these measurements, interleaved arrays of five infrared and five visible targets were fabricated on a common assembly, with a common background, a 4 x 8 foot sheet of Masonite painted black. Five 11.4 cm holes were cut through the Masonite on 45 *cm* spacings, and a 15 *cm* square hot plate was mounted behind each hole, approximately one meter behind the Masonite. The visible light sources were also mounted on the Masonite on 45 cm spacings, interleaved with the infrared targets. The visible targets were fabricated from clusters of 21 high-brightness LEDs emitting near 680 nm. The line through the centers of all targets was horizontal, one meter above the asphalt runway where the tests were performed. With discrete, electrically powered sources, both vertical and horizontal tilt components can be measured, and image contrast can be controlled by adjusting the brightness of the sources.

In the second case, we used an extended target with a clearly defined edge, and then analyzed the edge response. A similar approach was used in Ref. 8. Accordingly, an edge target was fabricated from a 4 x 9 foot sheet of white, high-density polyethylene foam by painting half of it black. The black-to-white edge was oriented horizontally. The edge had high contrast in the visible region when illuminated by the sun, and it also had contrast in the infrared because the black half of the foam became much hotter than the white half. However, the infrared contrast was never very high, it depended on the sun's position, and it was subject to rapid variations on days when clouds were present.

The measurements were performed at two sites. In August 2001, the field data were acquired at a closed runway at Fort Gillem, a US Army facility located in Forest Park, Georgia, which is in the Atlanta metropolitan area. The runway is approximately 950 meters long and 23 meters wide. The runway clearing extends several hundred meters to the south (with uneven terrain) and is bordered on the north by newly planted fir trees roughly 1 meter tall. The clearing is 150 meters wide at its narrowest location. About 75% of the western side of the runway is forested, with trees on only 40% of the eastern side. The ends of the runway appeared to be level with one another, but the center is lower than the ends. The airstrip has the dip near the center. This test site was chosen because it provided a line-of-site path approximately 1 km long as well as reasonably uniform surrounding terrain.

The targets were set up at the northern end of the runway. The dual-band imaging system, meteorological station, and a scintillometer were set up on the southern end of the runway. The air temperature, barometric pressure, wind speed and wind direction, as well as refractive index structure characteristic, C_n^2, were recorded. The scintillometer receiver was located 150 meters from the receiver. The data were collected from early morning until early evening on August 22-24, 2002. Several tens of sets of data including 10,000 data frames each were recorded at various time of the day with four aperture diameters and at two spectral wavebands. The sky was partially or completely clear during these days. Both PCs were equipped with 40 Gbyte hard disk drives and CD burners. The disk drives were large enough to record an entire day of data, and the CD burners were used to back up the data at the end of each day. Unfortunately, signals from the different read ports of the Electrim camera picked up noise on their way to the digitizer, and this resulted in the appearance of periodic noise. Consequently, a limited number of data sets acquired in the visible waveband were available for the data analysis.

The field measurements were scheduled for August-September 2001. However, after September 11, the Ft. Gillem site was not available due to an increased level of security. For this reason an alternate test site was located, at the Fulton County Municipal Airport. The alternate site was an unused runway, oriented east-west and very flat. The path length for the dual-band optical sensors in the September test was 732 m. The scintillometer was operated over a range of 300 m, parallel to the imaging path.

Tilt Statistics From Discrete Sources

Spatial Tilt Statistics

In the case of discrete IR sources, the analyses included the following steps. First, X and Y components of the image centroid were determined for each of five source images in each data frame. Second, the time series of the X and Y tilt components were derived from the sequence of 10,000 data frames. Third, the low frequency trends, if present, were removed from the time series. Then the tilt statistical characteristics including tilt structure function, tilt variance, tilt spatial and temporal correlation coefficients, and tilt power spectral density (PSD) were calculated. The results were compared with the theoretical predictions. The values of refractive index structure characteristic C_n^2 estimated from the imagery data were compared with those measured with the scintillometer.

The first statistical characteristic of an atmospheric tilt that we estimated from the field data was the tilt structure function, $D_{x,y}(\Delta\theta)$, which is defined by equation

$$D_{x,y}(\Delta\theta) = \left\langle \left[\varphi_{x,y}(0) - \varphi_{x,y}(\Delta\theta)\right]^2 \right\rangle = 2\sigma_{x,y}^{\,2}[1 - b_{x,y}(\Delta\theta)], \tag{1}$$

where $b_{x,y}(\Delta\theta)$ is the tilt angular correlation coefficient, $\sigma_{x,y}^2$ is the tilt variance, and $\Delta\theta$ is the horizontal angular distance between sources. The tilt structure function has several advantages, as compared to the tilt correlation function. First, the tilt structure function is insensitive to any sensor vibration because sensor motion causes a global image motion, which is cancelled in the difference in Eq. (1). Second, the tilt structure function directly characterizes the r.m.s. pointing error in the laser projection system under the condition that the imaging sensor and the laser projecting system have the same aperture diameter. Third, when $\Delta\theta$ exceeds the tilt correlation angle, $\Delta\theta > \theta_c$, the tilt structure function saturates at the constant level, which is equal to $D_{x,y}(\Delta\theta) \approx 2\sigma_{x,y}^{\,2}$. Therefore, for large angular distances $\Delta\theta$ one can obtain an estimate of the tilt variance $\sigma_{x,y}^2$ and therefore an estimate of the C_n^2, which is not affected by any sensor vibration. We used this property of the tilt structure function in our study. Finally, it is important to note that because tilt variance and the tilt correlation coefficient are wavelength independent, one can estimate the r.m.s. pointing error in a laser projection system by using the imagery data acquired at different wavelength.

Figure 1 shows structure functions of the longitudinal (X) and lateral, with respect to the separation between the discrete sources, (Y) tilt components versus angular distance between the sources. These structure functions were measured at various time of the day with *D*=6 cm aperture diameter. It is seen that from early morning until noon the tilt structure function for angular separation of 2 *mr* increases by about one order of magnitude. This behavior is consistent with the known diurnal cycle of C_n^2 near the ground.[9] For an angular distance of 1 *mr* (0.9 m at 950 m range) the r.m.s. tilt difference for the X (horizontal) tilt component at early morning is 7 *μrad*, whereas around noon it is 16 *μrad*. For an angular distance of 0.45 *mr*, the r.m.s. tilt differences at early morning and at noon are 5 *μrad* and 12 *μrad*, respectively.
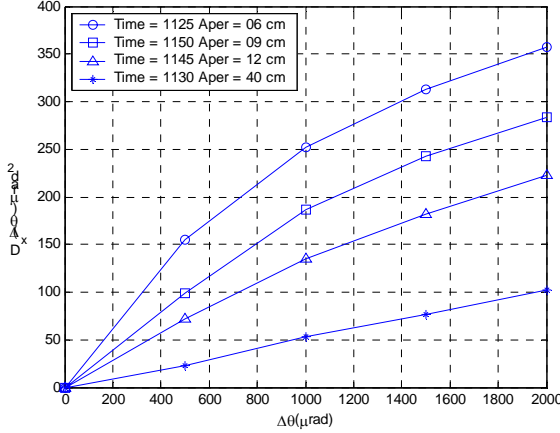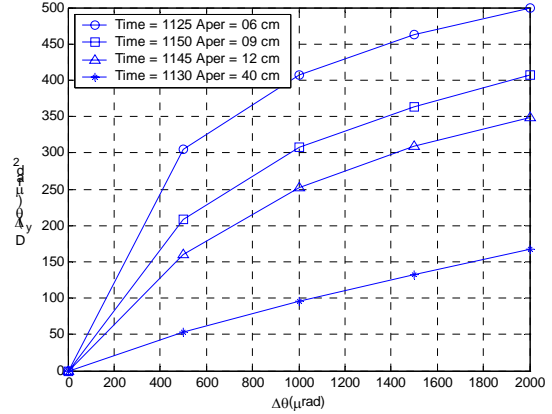
6
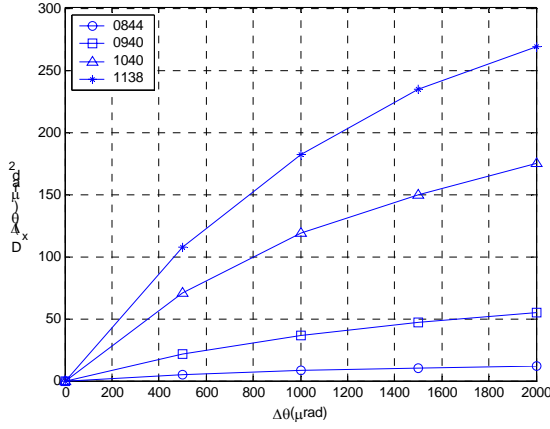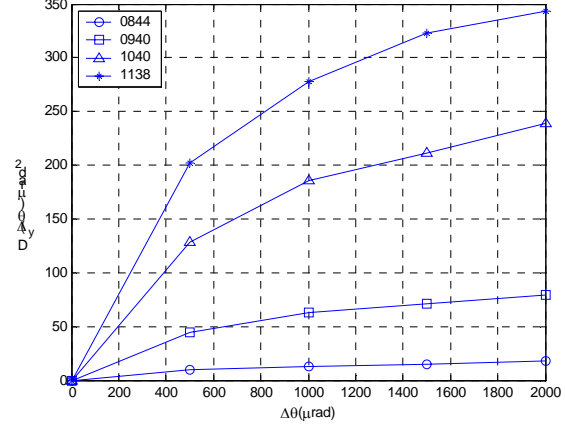
Figure 1 a and b. Structure functions of the longitudinal a) and lateral b) tilt components measured with discrete IR sources and aperture diameter D = 6 cm at various time of the day on August 24, 2001. The tilt structure function for angular separation of 2 *mr* increases by about one order of magnitude from early morning until noon.

Figure 2 illustrates the aperture averaging effect on tilt anisoplanatism. In this case the tilt structure functions, $D_{x,y}(\Delta\theta)$, were measured sequentially with aperture diameters of $D = 6$ cm, 9 cm, 12 cm, and 40 cm during a 25-minute time period from 11:25 am to 11:50 am. The tilt structure function gradually reduces with the aperture diameter *D*. For D = 6 *cm* and angular separation between the sources of 0.45 *mr*, the r.m.s. pointing error for X tilt is 12 *μrad*, whereas for *D*= 40 cm it is 5 *μrad*. The above r.m.s. tilt error characterizes the r.m.s. pointing error in tactical laser weapon systems for ground-to-ground engagement scenarios that have the aperture diameter of 0.5 m.

For small angular separations, $\Delta\theta \leq \theta_c$, the tilt structure function is reduced as D^{-1}. Consequently, the r.m.s. pointing error caused by tilt anisoplanatism is reduced as $D^{-1/2}$. The latter is due to two reasons: a) the tilt variance reduces with aperture diameter,[10] as $\sigma^2 \propto D^{-1/3}$, and b) the tilt correlation angle increases with the aperture diameter,[2,3] as $\theta_c \propto D/L$. One can also note that if the laser projection system operates at 1-micron wavelength and has an aperture diameter of 0.4 m, and the track point is separated from the aim point at the angle of 0.45 *mr*, then the r.m.s. pointing error caused by tilt anisoplanatism exceeds the diffraction limit for the laser projection system by a factor of 2.5. This suggests that the effect of tilt anisoplanatism must be corrected.

7

Figure 2 a and b. The effect of the aperture diameter on the structure functions of the longitudinal (X) and lateral (Y) tilt components measured with discrete IR sources on August 23, 2001. The tilt structure function gradually reduces with the aperture diameter D.

In Figure 3 we compare the measured data with the theoretical predictions.[3] Here the measured normalized X tilt structure function $D_N(\Delta\theta) = D_x(\Delta\theta)/D_x(2mrad)$ for $D = 6$ cm is shown versus normalized angular distance between the sources along with the theoretical prediction.[3] The angular distance between the sources was normalized to the tilt correlation angle. For $L = 902\ m$ and $D = 6\ cm$ the imager angular size is $\theta_D = 66\mu rad$. If the average height of the optical path above the ground is $h = 1.5$ m, then the outer scale of turbulence $L_0 = 0.4h = 0.6\ m$. Therefore, the normalized outer scale is $\gamma = L_0/D = 10$. Therefore, the correlation angle for the lateral (Y) tilt component is $\theta_{c,Y} = 660\mu rad$, whereas the correlation angle for the longitudinal (X) component is $\theta_{c,Y}/2 = 330\ \mu rad$. The measured normalized structure function agrees with the theoretical prediction. This confirms the theoretical prediction[3] that the tilt correlation angle is given by $\theta_c = \gamma(D/L)$.

At the same time, the ratio of the absolute values of the X and Y tilt structure functions in Figures 1 and 2, is inconsistent with the theory. According to the theory,[2,3, 11] the tilt structure function for the longitudinal (X) tilt exceeds the structure function for the lateral (Y) tilt $D_x(\Delta\theta)/D_y(\Delta\theta) > 1$ for all angular separations $\Delta\theta$. The latter is because the angular separation $\Delta\theta$ degrades the correlation of the horizontal (X) tilt more than the vertical (Y) tilt.[11] Meanwhile, in Figures 1 and 2 the tilt structure for the vertical tilt exceeds that for the horizontal tilt, $D_x(\Delta\theta)/D_y(\Delta\theta) < 1$. In order to explain this disagreement with the theory, we hypothesized that the heat from the IR sources created artificial turbulence near the source, which produced an additional contribution to the image motion. We validated this assumption by using the acquired imagery data.
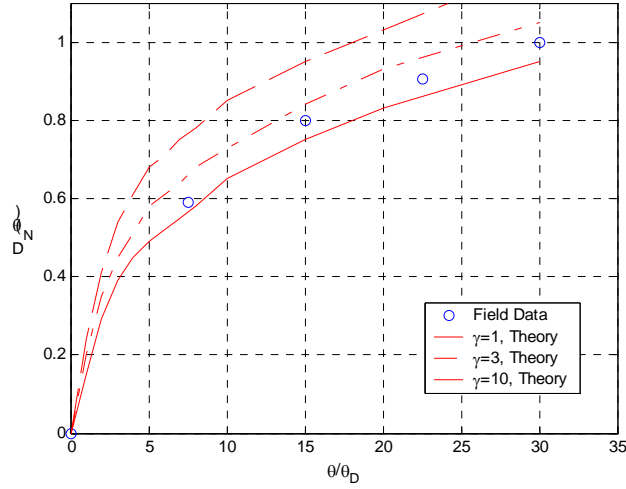
Figure 3. Comparison of the normalized tilt structure function measured with $D = 6$ cm with the theoretical prediction. The measured normalized structure function agrees with the theoretical prediction.

Figure 4 depicts the ratio of the X and Y tilt variances estimated from the tilt structure functions measured with D=6 cm on August 23 and 24, 2001. The tilt variances were calculated by using the expression $\sigma_{x,y}^2 \approx D_{x,y}(2mrad)/2$. Variance of the vertical (Y) tilt in Figure 4 exceeds variance for the horizontal (X) tilt by a factor 1.3-1.5, whereas in the isotropic turbulent atmosphere[10] the tilt variances are equal, $\sigma_x^2 = \sigma_y^2$. This confirms our hypotheses that the IR sources introduced an additional vertical tilt.
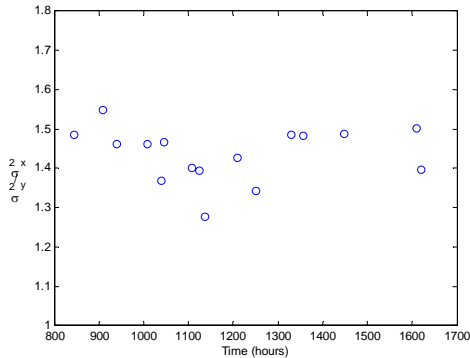
Figure 4. The ratio of the variances of the X and Y tilt components estimated from the tilt structure functions measured with discrete IR sources on August 23 and 24, 2001.
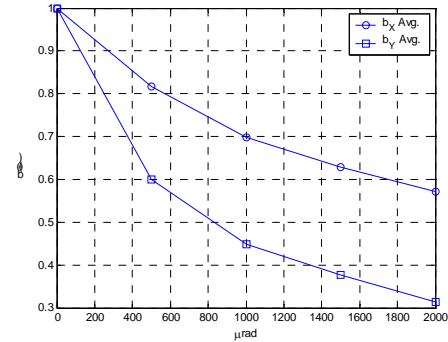
Figure 5. Correlation coefficients for X and Y tilt components measured with discrete IR sources and aperture diameter of 6 cm.

The average spatial correlation coefficients of the horizontal (X) and vertical(Y) tilts measured with D=6 cm are shown in Figure 5. The tilt correlation coefficients estimated from four data sets

acquired from 10:45 am until 16:09 pm were averaged together, and the average correlation coefficient curves are shown in the plot. The measured correlation coefficient for the longitudinal (X) tilt exceeds that for the lateral (Y) tilt, $b_x(\Delta\theta) > b_y(\Delta\theta)$, whereas the theoretical prediction is $b_x(\Delta\theta) < b_y(\Delta\theta)$.   This result also confirms our assumption regarding the contribution of the IR sources on the vertical tilt. The contribution from the heat-induced turbulence reduces spatial correlation of the vertical (Y) tilt. Both tilt correlation coefficients have large DC components, which is most likely due to the sensor vibration.

The X and Y tilt variance measured with various aperture diameters and normalized to the variance for D= 6 cm are shown in Figure 6. Four data sets recorded from 9:16 am until 14:52 pm on August 23, 2001 were averaged and are shown in this plot. The theoretical prediction for an infinite outer scale,[10] $\sigma_\varphi^2 \approx D^{-1/3}$ is also shown. The normalized variance for the horizontal tilt agrees well with the theoretical curve, whereas the variance of the vertical tilt has a steeper than $D^{-1/3}$ slope. The latter could be due to the effect of the heat-induced turbulence, or the finite vertical turbulence outer scale.

Finally, in Figure 7 we compare the C_n^2 values measured with the scintillometer with the values estimated from the structure function of the longitudinal (X) tilt measured in August 23 and August 24, 2001. The C_n^2 values retrieved from the measurements with two independent optical sensors agree well. On August 23 the C_n^2 values are in the range $6\cdot10^{-14} m^{-2/3} \leq C_n^2 \leq 5\cdot10^{-13} m^{-2/3}$, whereas the C_n^2 range on August 24 is $2\cdot10^{-14} m^{-2/3} \leq C_n^2 \leq 3\cdot10^{-13} m^{-2/3}$. On August 24 the scintillometer data exhibits stronger temporal variations than the data from the dual-band imager. The latter could be due to the difference between optical path lengths: L= 902 m for the imager, and L=150 m for the scintillometer.
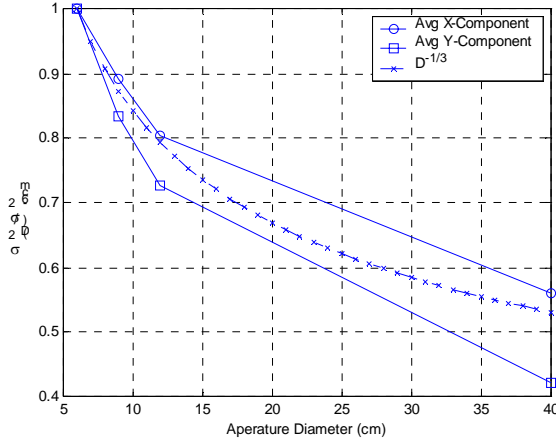

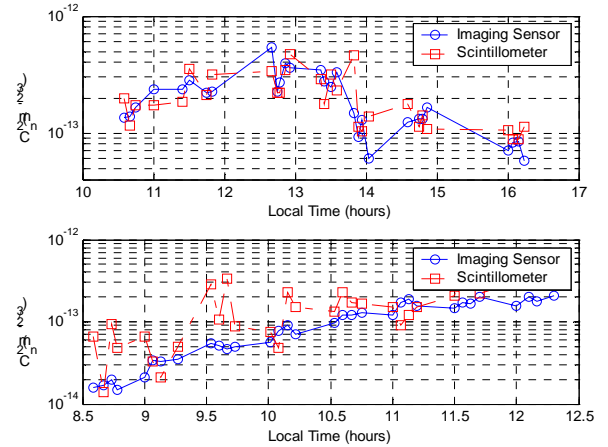Figure 6. Normalized variance of the horizontal(X) and vertical (Y) tilt components versus aperture diameter.

Figure 7. Comparison of the values of C_n^2 retrieved from the imagery data with the readings from the scintillometer.

10

Temporal tilt Statistics

Tilt temporal statistics were also retrieved from the field data acquired with discrete sources. Figure 8 shows the power spectral densities (PSDs) of the longitudinal (X) tilt measured with apertures $D=$ 6 cm and $D=$ 40 cm. In the low frequency range the PSD has the "-2/3" slope, which is consistent with the theoretical prediction.[10] Also, the PSD for the small aperture exceeds that for the large aperture. The knee frequency, where the PSD changes slope, for $D=$ 40 cm is about 2 Hz, whereas for $D=$ 6 cm it is 13 Hz. The wind velocity estimated from the knee frequency, $f_k = \dfrac{0.33 \cdot V}{D}$, for $D=$ 40 cm is $V=$ 2.4 m/sec, whereas for $D=$ 6 cm it is $V=$ 2.3 m/sec. The ratio of the two knee frequencies $f_{k1}/f_{k2} = 13Hz/2Hz = 6.5$ is equal to the inverse ratio of the corresponding aperture diameters $D_2/D_1 = 40cm/6cm = 6.6$. The implication is that the measured PSDs are consistent with the theory.[10]

Temporal correlation coefficients of the horizontal (X) measured with D=6 cm aperture and D= 40 cm are shown in Figure 9. These curves were obtained by averaging correlation coefficients $b_x(\Delta\theta)$ computed from 7 data sets recorded from 10:45 am to 16:09 pm on August 23, 2001. The tilt temporal correlation increases with the aperture diameter. The tilt temporal correlation scale defined as the time duration over which the correlation coefficient decreases to the e^{-1} level, is 0.2 sec for D=6 cm, whereas it is about 1 sec for $D=$ 40 cm.

Figure 10 compares temporal correlation coefficients of the horizontal (X) and vertical (Y) tilt computed from the same 7 data sets recorded with D=6 cm aperture from 10:45 am to 16:09 pm on August 23, 2001. Once again, it is seen that the temporal correlation scale for the horizontal (longitudinal) tilt exceeds that for the vertical Y-tilt, whereas according to the theoretical prediction, this should be the inverse. This result is also consistent with our assumption that the heat –induced turbulence degraded the measurements of the vertical (Y) tilt.
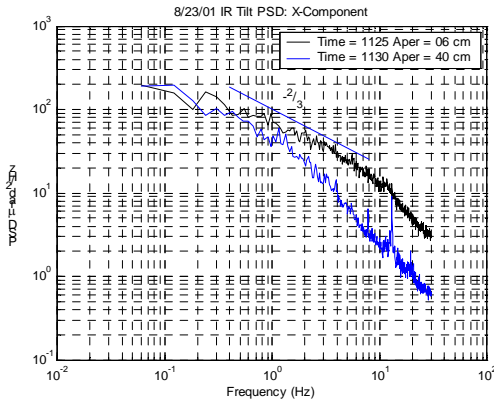

Figure 8. Power spectral density measured with the aperture diameter of 6 cm and 40 cm.
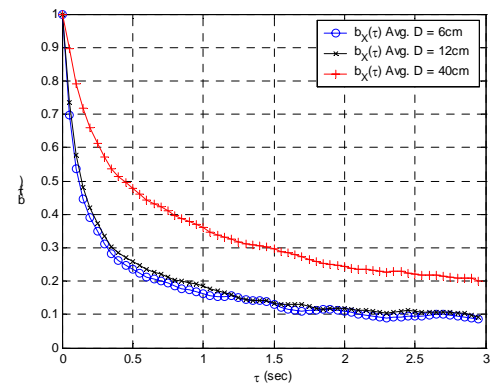

Figure 9. Temporal correlation coefficients of the horizontal (X) tilt measured with D = 6 cm, 12 cm, and 40 cm.
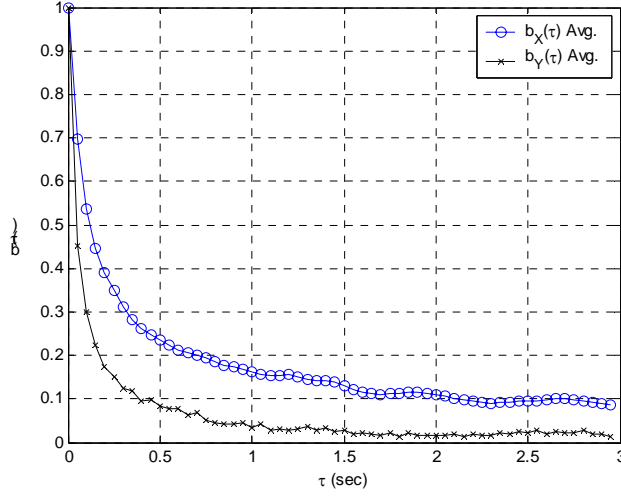
Figure 10. Temporal correlation coefficient of the longitudinal (X) and lateral (Y) tilt measured with D=6 *cm* aperture from 10:45 am to 16:09 pm on August 23, 2001.

Tilt Statistics From an Extended Object

The tilt statistics were also estimated from the edge measurements with an extended object. The edge detection was performed by using a threshold approach similar to that in Ref. 8. First, the transition zone was found for each pixel column in the frame, where the brightness gradually increases. Then the brightness level at the lower and upper boundaries of the transition zone, denoted T_1 and T_2, respectively, were determined along with the threshold $(T_2 - T_1)/2$. After that the threshold algorithm was applied to determine the edge position for a given column. This procedure was applied to all data frames in the data set. Once all 10,000 data frames are processed, the edge statistics, or statistics of the vertical (Y) tilt were calculated.

Figure 11 shows the edge, or vertical (Y) tilt, structure function measured with D= 6 *cm* aperture from 8:44 am until 10:04 am. The edge structure function change over time is consistent with the known diurnal cycle of C_n^2, as well as with the tilt structure function behavior in Figure 1 measured with discrete sources. (Day, visible or IR)

Figure 12 depicts the edge structure functions measured sequentially with aperture diameters of $D =$ 6 cm, 9 cm, 12 cm, and 40 cm during a 20 minute time period at early morning. The absolute values of the edge structure function are close to that in Figure 2. Similarly to that in Figure 2, the edge structure function is gradually reduced with *D*. For small angular separations, $\Delta\theta \le \theta_c$, the edge structure function is reduced as D^{-1}.
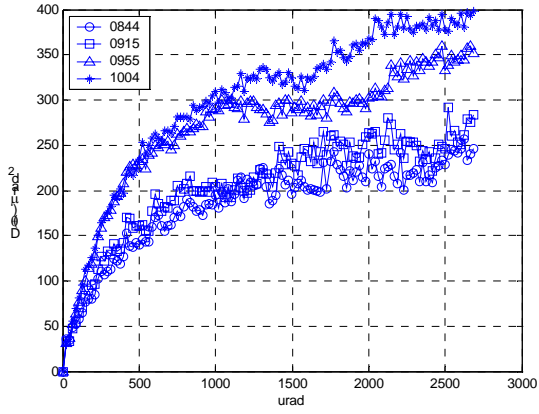
Figure 11. Edge structure function measured with an extended source and 6 cm aperture from 8:44 am until 10:04 am.
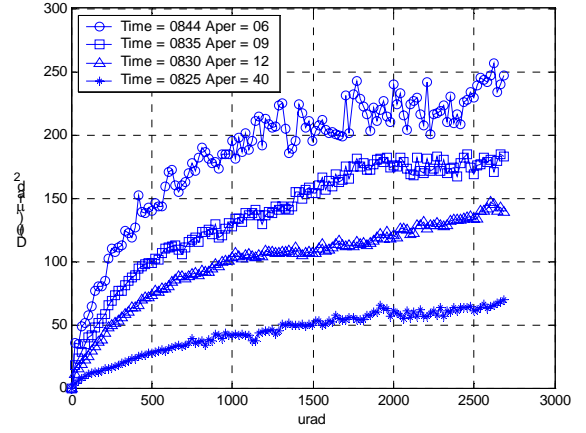

Figure 12. Edge structure function measured with an extended source and aperture diameter of $D = 6cm$, $9cm$, 12 cm, and 40 cm .

13

Finally, Figure 13 compares the normalized edge structure function $D_{x,y,N}(\Delta\theta) = D_{x,y}(\Delta\theta)/D_{x,y}(2.6mrad)$ measured with D= 9 cm and D= 12 cm with the theoretical predictions that corresponds to different normalized turbulent outer scale $\gamma = L_0/D$. One should note that when the structure functions measured at different times of the day and under various turbulence conditions are normalized to the maximum values, they all converge to a single universal curve with very small variations. This confirms the theoretical prediction that the tilt correlation angle is determined by the angular size of the imager, $\theta_c \propto D/L$, and is independent of the strength of turbulence along the path.

Both field data acquired with both discrete and extended sources, in particular data presented in Figures 1, 2, 11, and 12 allow one to estimate the r.m.s. pointing error caused by anisoplanatism of the aim point to the track point on a horizontal path in both weak and strong turbulent conditions.

Mitigation Technique of Edge Image Waviness

Because turbulence-induced tilt anisoplanatism degrades the performance of both laser projection and optical imaging systems, it is important to mitigate this effect. Three approaches can be employed to reduce the impact of tilt anisoplanatism on electro-optical systems. The first approach is based on the fact (see Figures 2 and 12) that the tilt structure function, which characterizes tilt anisoplanatism, reduces with the aperture diameter. Therefore, by increasing the transceiver aperture one can reduce the r.m.s. pointing error in the laser projection system, or the edge image waviness in the imaging system. However, in some applications the maximum aperture diameter is limited. In this case, alternative approaches should be considered.
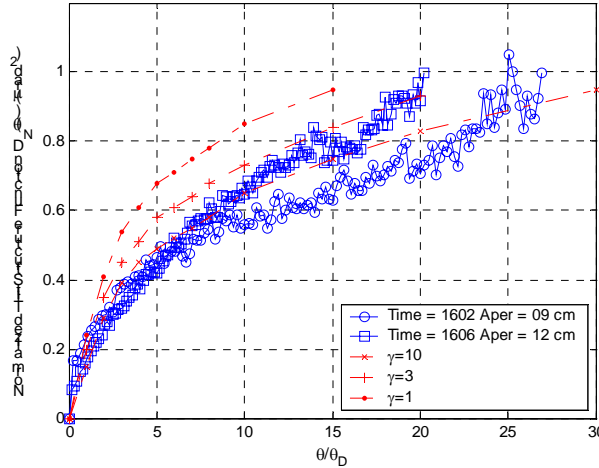
Figure 13. Comparison of the measured normalized edge structure function with the theoretical predictions. . This confirms the theoretical prediction that the tilt correlation angle is determined by the angular size of the imager, $\theta_c \propto D/L$, and is independent of the strength of turbulence along the path.

The second mitigation technique is based on integration of the instantaneous edge along the object angular extent. This approach was evaluated in Ref. 3. Also the same concept was used in the scheme for measuring a wavefront tilt from a laser guide star to reduce the undesirable contribution of the downlink path to the measured tilt.[2,12] In this method the edge position is integrated along the object and edge angular extent. The integrated edge position is defined by

$$\bar{e} = \frac{1}{\theta_R} \int_0^{\theta_R} e(\theta) d\theta \tag{2}$$

14

where θ_R is the object angular extent. If the object angular extent exceeds the tilt correlation scale, $\theta_R > \theta_c$, then the r.m.s. edge error is reduced. Figure 14 compares the edge averaging function computed directly from the edge time series and corrected for the sensor motion with the theoretical prediction.[3] The correction was done in the same way as that in Ref. 3. The correction is based on comparison of the edge variance estimated from the edge structure function, which is not affected by sensor vibration, with the edge variance computed directly from the edge time series that includes the contribution of the sensor vibration. The corrected edge averaging function agrees with the theoretical prediction.

This approach is efficient when an object has large angular extent, $\theta_R > \theta_c$, like in the laser guide star case, when it is viewed through an auxiliary telescope. However, in many applications it is not the case.
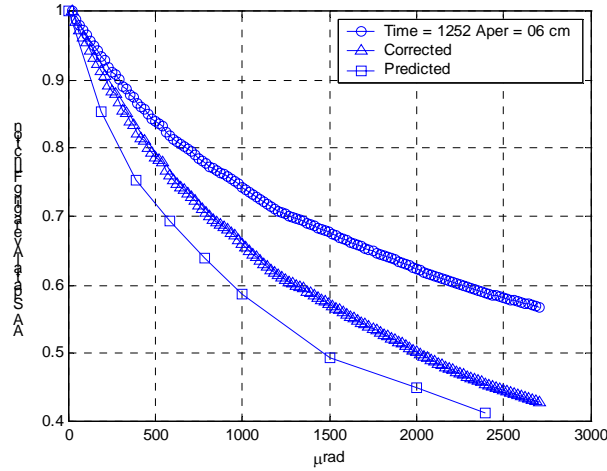

Figure 14. Comparison of the edge averaging function computed directly from the edge time series (uncorrected) and corrected for the sensor vibration with the theoretical prediction. The corrected edge averaging function agrees with the theoretical prediction.

The third approach uses temporal integration or summing up of multiple data frames. This approach is attractive because multi frame summation is also used in various applications to reduce the effect of turbulence-induced scintillation in the laser illuminating beam and laser speckles on the optical image. This approach is considered in the next section

Target Edge Response and Multi-Frame Summation

Figures 15 and 16 illustrate the multi-frame summation approach. Figure 15 shows an image of an extended IR source in a) single frame image, and b) multiple (100) averaged frames acquired with D=6 cm. Figure 16 presents similar results for an extended visible source.

It is easy to see that the image edges appear wavy in a single frame image, whereas in the multi-frame averaged image the edges are straight. Similar results were obtained with D = 9 cm, 12cm, and 40 cm. These results provide clear evidence that multi-frame summation mitigates the effects of tilt anisoplanatism. The implication is that multi-frame averaging efficiently reduces three effects: a) tilt anisoplanatism, b) laser speckle, and c) turbulence-induced scintillation in a laser illumination system.
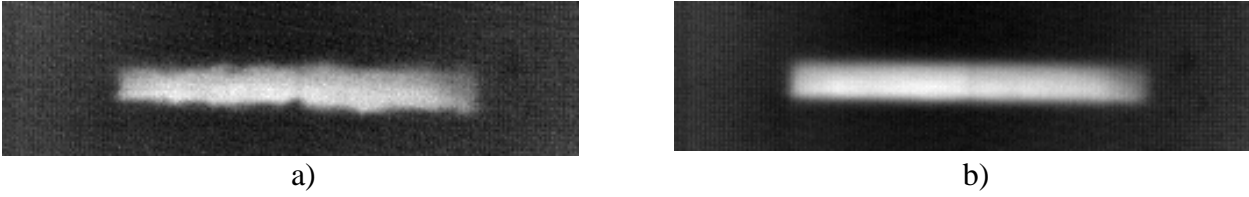
15

a)   b)

Figure 15. A single frame image a) and multi-frame (1000 frames) average image b) of an IR extended object

a)   b)

Figure 16. A single frame image a) and multi-frame (100 frames) average image b) of a visible extended object

It was expected that multi frame summation, or longer exposure time, will blur the image and change the target edge response. Figures 15 and 16 reveal that the edge response, or the image brightness profiles in the transition zone between the source and a background, is the same for a single frame image and multi-frame summed image. Figure 17 shows the edge responses for a single frame image and multi-frame summed images shown in Figures 15 and 16. Figure 17 provides clear evidence that a multi frame summation does affect the edge response, or target edge response is independent of an exposure time.

Finally Figure 18 shows the edge responses for single frame and multi-frame average visible and IR images acquired on August 27, 2001 at 13:42 am with D=40 cm. Once again the edge response for a single frame image and multiple frames summed image is the same. The estimated atmospheric coherence diameter, or Fried parameter, for L=732m and maximum strength of turbulence in the visible is $r_0 = 3mm$. Therefore, the ratio $D / r_0 = (40cm) / 3mm = 133$. At the same time, this parameter in the IR waveband is $r_0 = 77.5cm$, and $D / r_0 = 0.77 < 1$. Thus the edge response for an extended object is invariant with respect to a multi-frame summation, or exposure time. This means that one can mitigate the effects of tilt anisoplanatism, laser speckle, and turbulence-induced scintillation by summing up multiple frames without losing angular resolution. This new finding is important for practical applications. This result, to the best of our knowledge, has not been reported in the literature. A refereed journal paper that provides a theoretical interpretation for the above property of the target edge response is in preparation. A conference paper that summarizes the new experimental finding has been accepted for presentation at the SPIE Meeting in Denver, Colorado in July 2004.

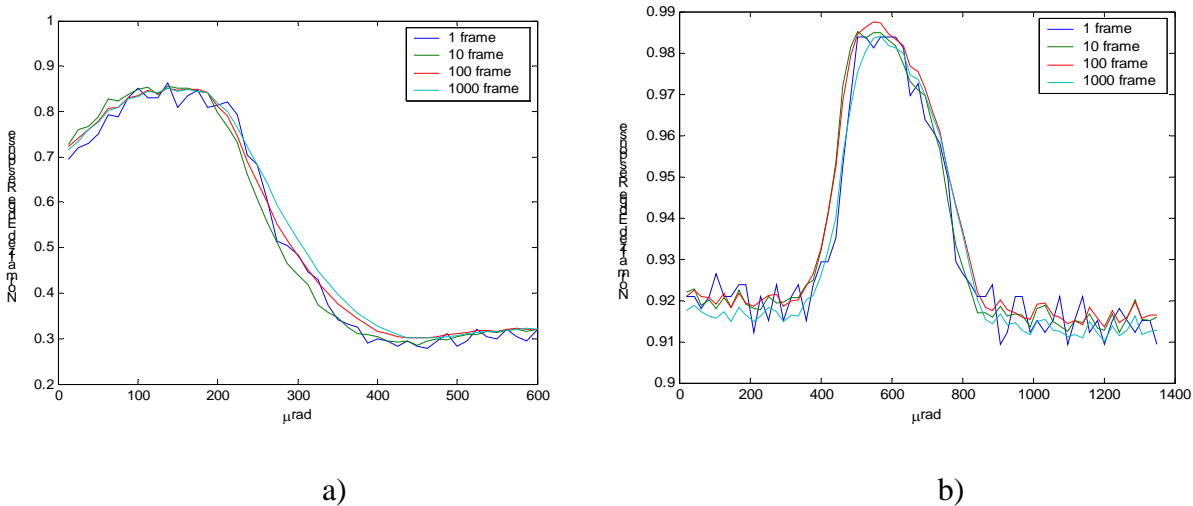a)   b)

Figure 17. Edge responses in a single frame image, and multi-frame averaged image for an extended visible source a) and IR source b) measured with aperture diameter D= 6 cm .
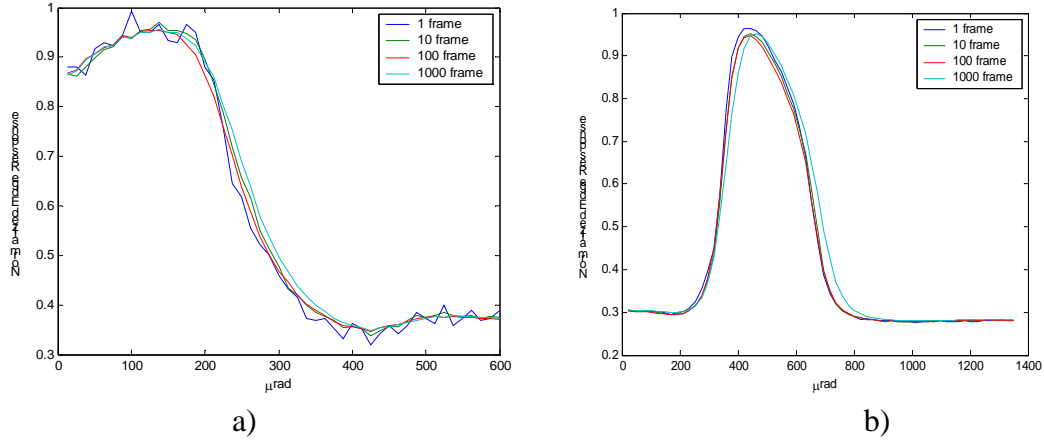
Figure 18. Edge responses in a single frame image, and multi-frame summed image for an extended visible source a) and IR source b) measured with aperture diameter D= 40 cm .

Conclusions

From the experimental imaging study, the following conclusions can be made:

1.   Tilt anisoplanatism degrades the performance of a laser projection in the same way as it impacts an image of an extended object in an optical imaging system. This allows us to estimate the r.m.s. pointing error caused by anisoplanatism of the track point to the aim point in the laser projection system from the imagery data acquired with a passive optical sensor having the same aperture diameter as the laser projection system.

2.   Wavefront tilt statistics, including tilt anisoplanatism, are wavelength independent. Therefore, one can estimate the r.m.s. pointing error caused by tilt anisoplanatism in a laser projection system by using imagery data acquired in a different spectral waveband.

3.   A dual-band imaging system with variable aperture diameter was built and atmospheric tilt was measured on a 1-km near-the-ground horizontal path using discrete and extended visible and IR sources. The spatial and temporal tilt statistics were estimated from the recorded data.

4.   The tilt structure function, which characterizes the variance of the pointing error caused by anisoplanatism in a laser projection system, is insensitive to sensor vibration, and for small angular separations it decreases inversely proportionally to the aperture diameter D^{-1}.

5.   The normalized tilt structure function measured with both discrete and extended sources agrees well with the theoretical predictions. This fact confirms that the tilt correlation angle is determined by the angular size of the aperture and is independent of the strength of turbulence.

6.   The values of the structure characteristics C_n^2 retrieved from the imagery data agree well with measurements from the scintillometer.

7.   The tilt temporal correlation scale for the aperture diameter of D= 6 cm and D= 40 cm is in the range from 0.25 sec to 1 sec, respectively

8.   The measured tilt power spectral densities agree well with the theory. They have the

"-2/3" power slope, and the ratio of the two knee frequencies for small and large aperture equals the inverse ratio of the corresponding aperture diameters.

9.   Three mitigation techniques for tilt anisoplanatism were considered. They include an increase of the aperture diameter, integration of the image edge over the edge angular extent, and averaging of multiple frames. The latter technique is known to be efficient for mitigation of the effects of turbulence-induced scintillation and laser speckle. We found that multi frame averaging efficiently mitigates the effects of tilt anisoplanatism on the image of an extended object as well.

10.   The target edge response for single frame and multi-frame summed images was investigated. We found that the edge response is independent of the multi-frame summation, or exposure time. The edge response for a single frame image and multiple-frame summed images is the same. This allows us to mitigate the effects of tilt anisoplanatism, laser speckle, and turbulence-induced scintillation by summing up multiple images without losing angular resolution. This new finding is important for many practical applications.

II. Purpose 2: Effect of Turbulence on Atmospheric MTF

Motivation
A separate goal of the research performed by the research team was to analyze the effect of turbulence on the Modulation Transfer Function (MTF) of the atmosphere along a horizontal path. The MTF of an optical system (in this case, the atmosphere) gives an objective measure of the system's ability to transfer object contrast and it is reported over a range of spatial frequencies. As such, it is a quantitative measure of the quality of an optical system. In the case of long-path outdoor imaging, the atmospheric MTF can be the limiting factor in the quality of images obtainable with military surveillance and targeting systems.

Optical Sensors and Experiment

On November 7, 2002 MTF measurements were conducted in the visible and the mid-wave IR. The measurements were images of point targets at a distance of 791m. Both the imagers and the targets were 1 meter off the ground. The visible imager consisted of a Point Grey Dragonfly CCD camera attached to an 8.13-m focal length telescope. The IR imager was made up of a Cincinnati Electronics TV-8500 3-5µm camera with a 4.02-m focal length optical system.

Both the IR and visible measurements were long exposure measurements in the sense that 255 frames of data collected at 30 fps were averaged to obtain the images that were later analyzed.

Our method for measuring the atmosphere's MTF was based on images of distant point targets. One line of pixels through the center of each image yielded the Point Spread Function (PSF). The Fourier transform of the PSF provides the MTF. However, this MTF is of the complete imaging system, which is made up of the atmosphere and the imager. The effect of the imager had to be divided out in order to obtain the MTF of the atmosphere alone. In order to insure that we were removing the effect of the imager in its exact state during data collection, the imager MTF was measured in the field immediately before target images were recorded. A plane mirror was placed in front of each optical system, and images were collected of the double-pass reflection of a built-in slit coupled to the focal plane of the imager. The validity of this process was confirmed in the laboratory under controlled conditions, imaging an external slit target in a single pass through each system.

Visible data for this test was collected with a Point Grey DragonFly camera. The target was a Helium-Neon laser placed at the far end of the measurement range and pointed directly at the imaging system.

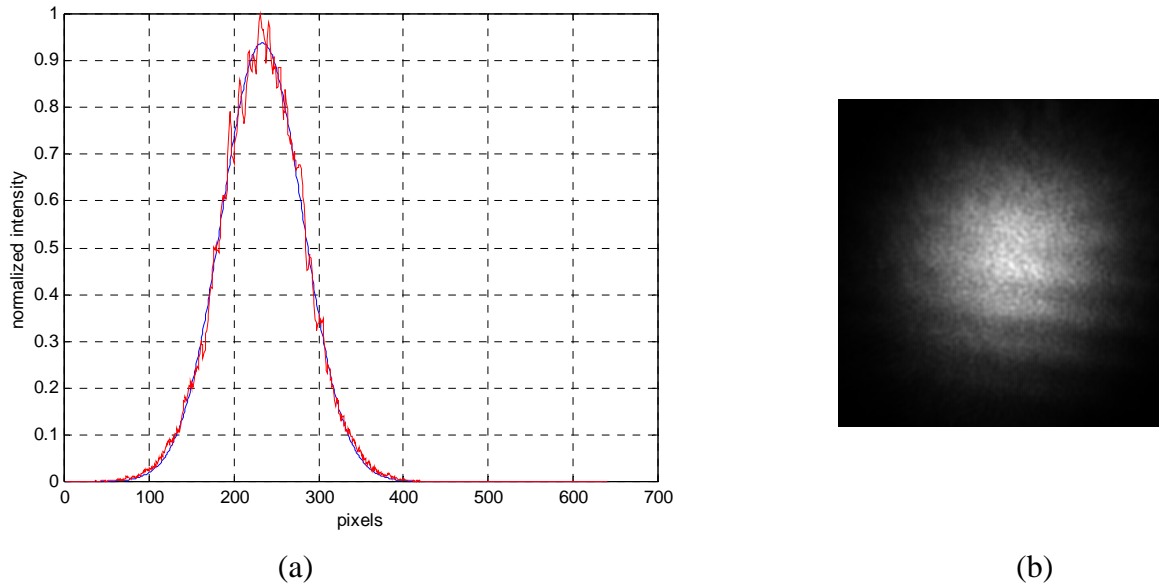(a)   (b)

Figure 19. (a) Pixel values from a horizontal slice through the center of the visible image
(b) The image of the visible point target

The image above was taken by the system. The red curve on the graph represents a horizontal slice through the image. The blue curve is a generalized least squares Gaussian fit to the profile. The raw data for both was pre-processed with background removal and normalization steps prior to the fit. The background was calculated from a "dark" region of the image as the mean + 3 standard deviations of the pixels in the region. The background was then subtracted from the resulting profile and all pixels with values less than zero were set to zero. Next the raw data was multiplied by 1/max(data[]) to normalize the maximum to 1. The Matlab 5.2 function fminsearch() was used to find a Gaussian fit to the curve. The same process was applied to imager MTF slit measurements taken in the field.

The next step was to calculate the imager MTF from the field slit measurement. The Gaussian fit to the slit measurement data was converted to an MTF with a Fast Fourier Transform (FFT) and divided by the analytical slit response.

Finally, the background subtracted raw data was transformed to an MTF and divided by the imager MTF. Visible data representative of high and low turbulence cases is plotted below.
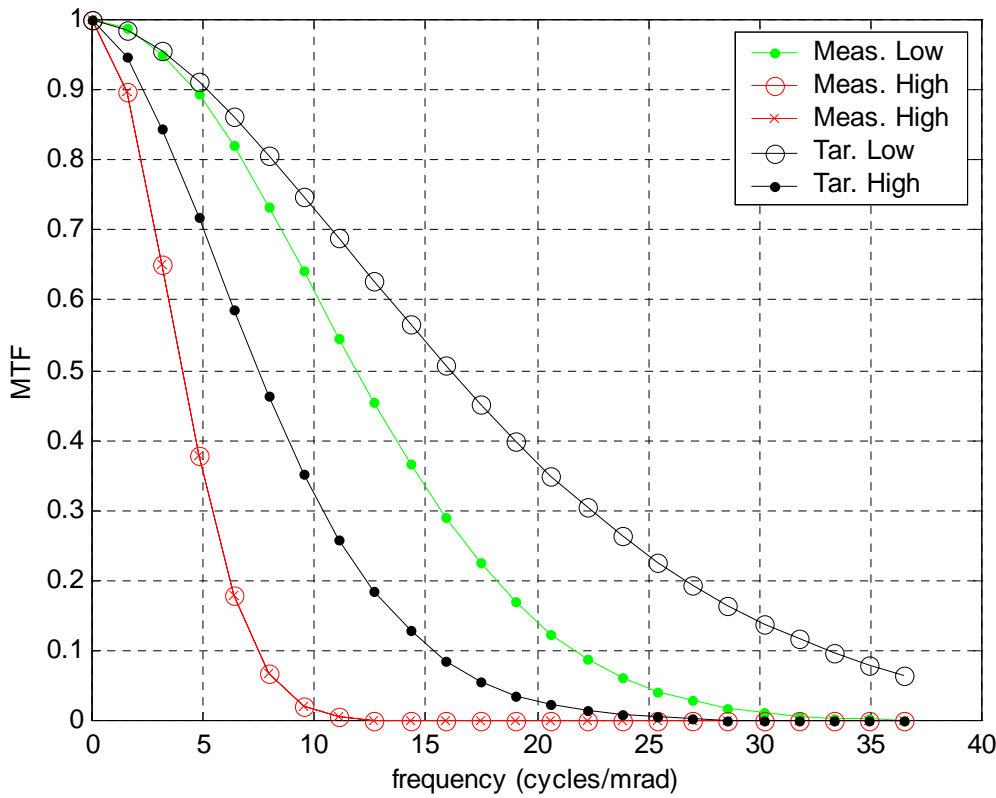
Figure 20. Atmospheric MTF from the visible imager in high nad low turbulence

For comparison purposes, the measured MTF values are compared to the theoretical curves for long exposure turbulence MTF.

$$\mathrm{MTF}_{LE} = \exp\left(-57.4\, a \cdot \xi^{\frac{5}{3}} \cdot C_n^{\ 2} \cdot \lambda^{\frac{-1}{3}} \cdot R\right)$$

$C_n^{\ 2}$ is the index of refraction structure parameter in m$^{-2/3}$, l is the wavelength of light in meters, R is the range in meters, and a is the waveform constant. a=3/8 for a spherical wave, and a=1 for a plane wave. $C_n^{\ 2}$ values used in the equations were taken from 5-minute averages measured by an Optical Scientific model LOA-004-AR scintillometer set up along the camera-to-target path. $C_n^{\ 2}$ was 1.3x10^{-13} m$^{-2/3}$ for the high turbulence cases and 3.6x10^{-14} m$^{-2/3}$ for the low turbulence cases. A spherical wave was used for the waveform constant, and R was 791m.

Results - Infrared MTF:
The target for this measurement was a blackbody set to 980°C with a 20-mm aperture.

The horizontal field of view of the IR camera and telescope was 1.91 mr, so the sample IFOV was 1.91/256 = 7.5µrad. The same analysis used for the visible images was applied to he IR images and the measured atmosphere MTF functions are shown below. The camera's peak response wavelength of 4.2µm was used to compute the theoretical MTF curves plotted with the measurements.

The analysis started by directly re-processing proprietary format IR video files into Matlab. During the test, the TVS-8500 camera was set up to save data at 15Hz and these files were post- processed.
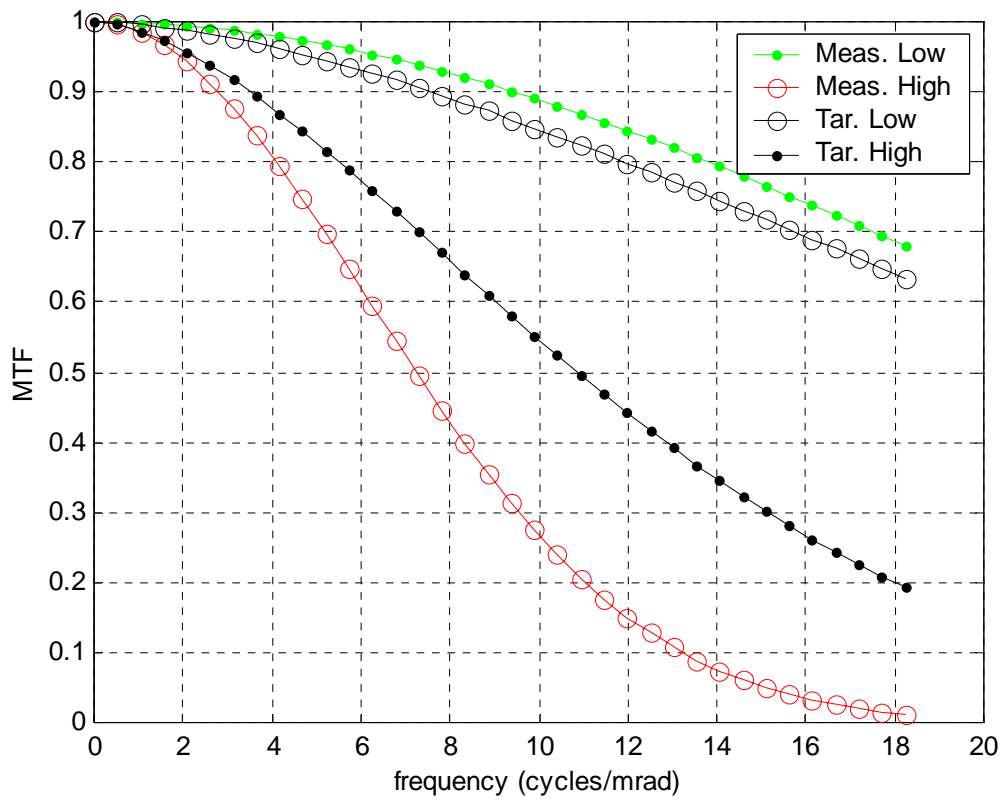
20

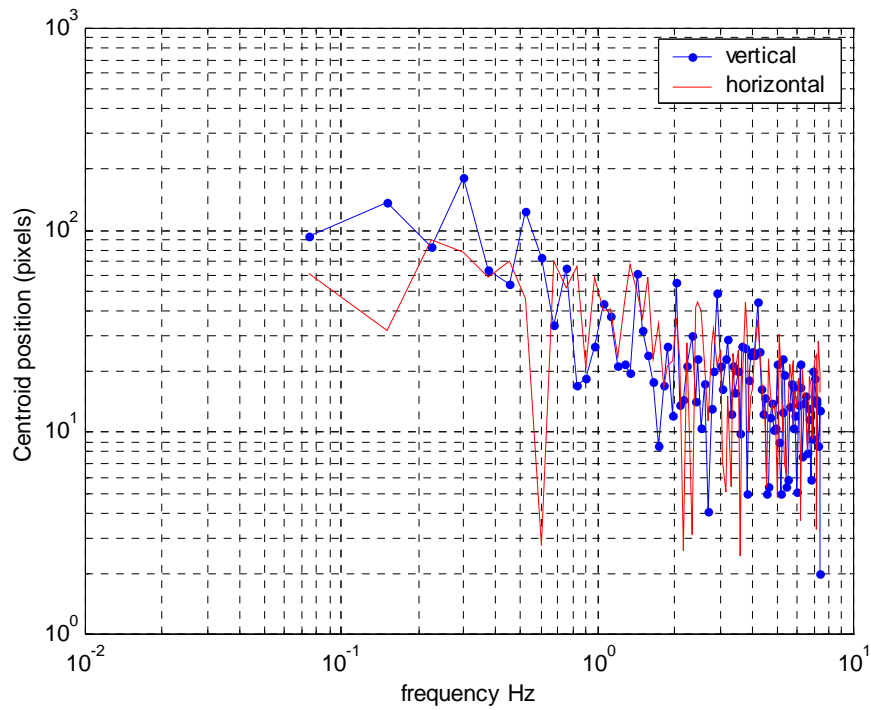Figure 21. Atmospheric MTF from the IR imager in high nad low turbulence .

Figure 22. IR point source target centroid position motion in the frequency domain.

Under high turbulence our measured MTF is narrower than the model predicts for the turbulence MTF alone. In order to get more insight into this problem, centroids of the target were computed for each frame. For each frame, the background was computed as the mean + 3 standard deviations of the pixels in the first 4 rows. A single bad pixel was zeroed in the image and then horizontal and vertical centroids were computed. The time data was then converted into the frequency domain and plotted on a log/log scale in Figure 22.
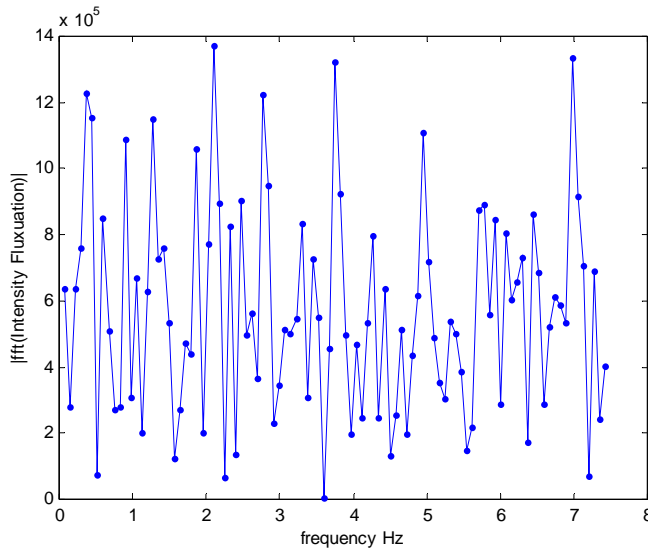

Figure 23. IR source intensity fluctuation in the frequency domain.

Another indicator of data quality is the change in intensity of the source verses time. The 8-inch diameter of the IR telescope and 20 mm diameter of the target are both large compared to the 6 mm inner scale of turbulence measured during the tests, so intensity fluctuations should be low. The normalized fluctuation in intensity for the low turbulence σ_I/μ_I^2 case was .023 and for the high turbulence case it was .0787. The power spectrum of the data is plotted to the right, and the intensity variation is flat across the frequency domain for both high and low turbulence cases. Hill and Ochs derive a formula that relates log amplitude variance of a source caused by scintillation for an extended target and a point receiver [J. Appl. Opt 17, 3608]. Using a target diameter of 8 in., the measured ratio of fluctuation is higher than the value predicted by the derived formula by a factor of 1.5.

Test of Calibrated MTF:
One row of the image was taken for each slit measurement. Multiple rows could have been used; however, the slit was not quite vertical in the image, so a method to compensate for the tilt would have been required. The Gaussian fits of the two slit images taken at 17:20 and 16:17 are essentially the same indicating the MTF was relatively stable. In Figure 24, both fits are shown along with the line spread data used for the 17:20 fit. The low amplitude halo near the bottom affects the fit, causing the amplitude of the Gaussian to be about 20% less than the data for the imager MTF. In a comparison of profiles through the atmosphere, the halo seemed worse in the system calibration sets. To eliminate the difference between calibration halo and the halo from the target measurements, the MTF calculation was repeated both for the system calibration and the field point sources with a background removal of 6σ. The 6σ background level caused the Gaussian fits to match the peak heights much more closely. Thresholding at the 6σ level worked out to be close to the 1/e level on the point spread curves.
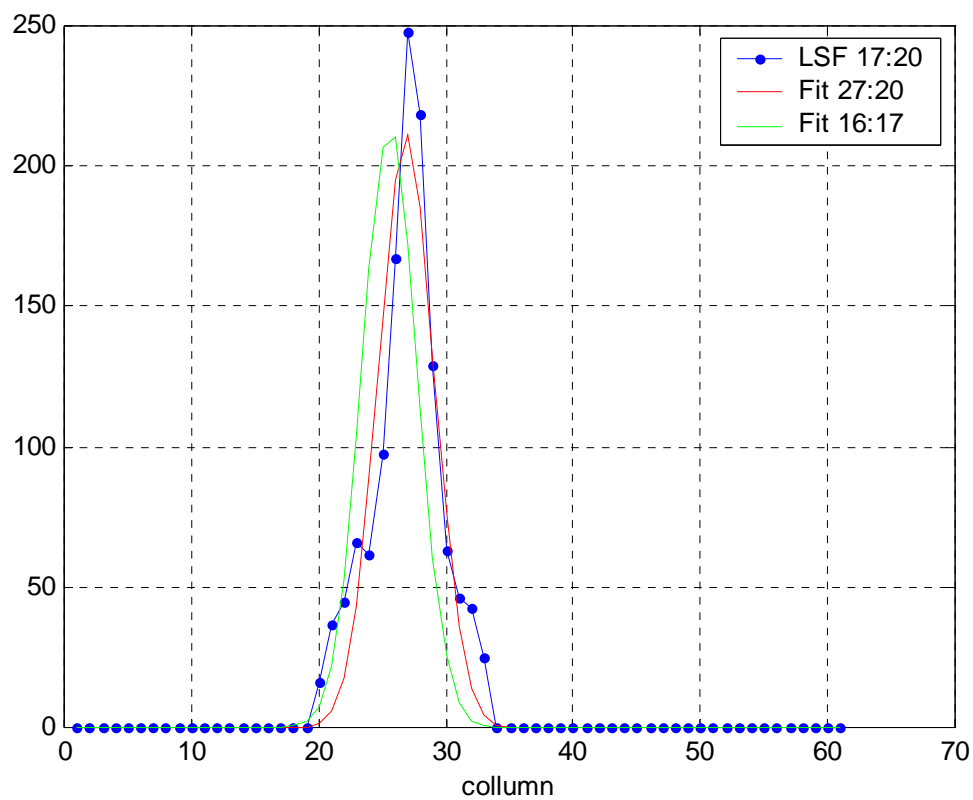
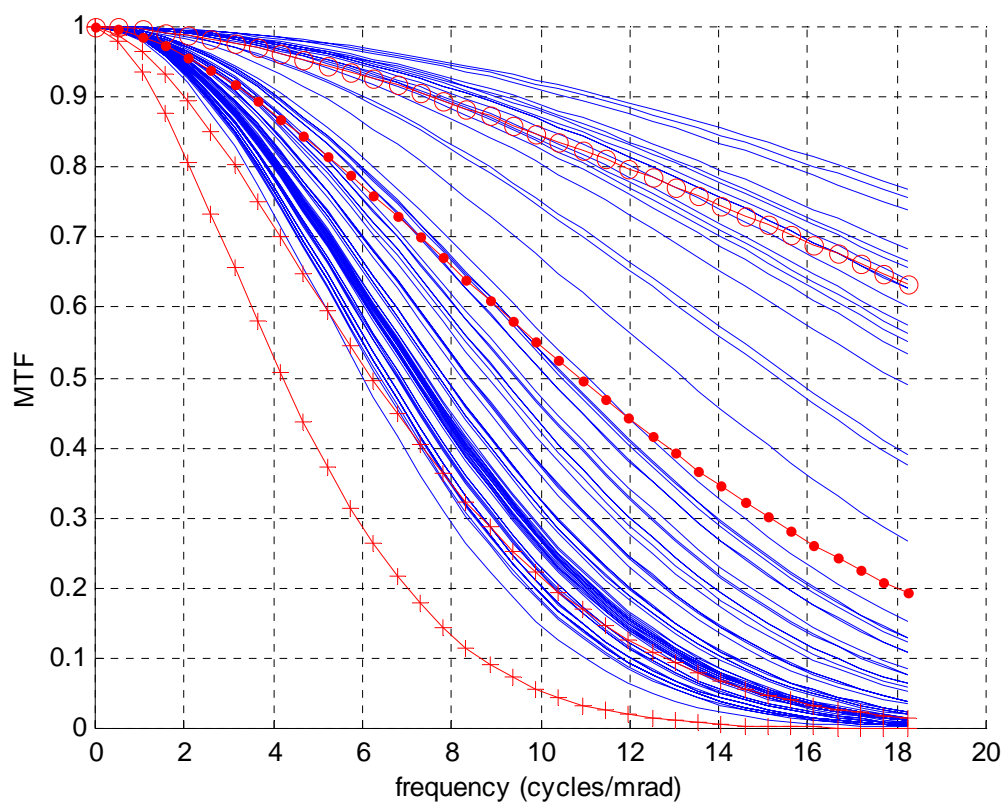Figure 24. Measured line spread data and best fit Gaussian curve.

Figure 25. Measured MTF values vs. theory.

Using the 6σ threshold, all 72 measurements were used to compute corrected MTF curves. Each computed MTF is shown in blue with no markers. The red plots represent different theoretical values for MTF verses C_n^2. The two curves marked with + represent C_n^2 values of 6.6×10^{-13} and 3.3×10^{-13}, the curve marked with points represents a C_n^2 of 1.3×10^{-13} which was the average during the high turbulence part of the day, and the curve marked with o corresponds to a C_n^2 of 3.6×10^{-14}. In general measured MTF curves are narrower than the theoretical curves based on C_n^2 measured with the scintillometer. Scintillometer reading were generated every 10 seconds and typical differences from sample to sample are 10%. The wider theoretical curve marked with + signs is more than 100% of the C_n^2 values that were typical during the high turbulence times of the day.

The MTF did track the C_n^2 readings from the scintillometer. Both are plotted below. As C_n^2 decreased, the MTF Full Width at Half Maximum (FWHM) increased, showing improved atmospheric imaging quality with reduced turbulence.
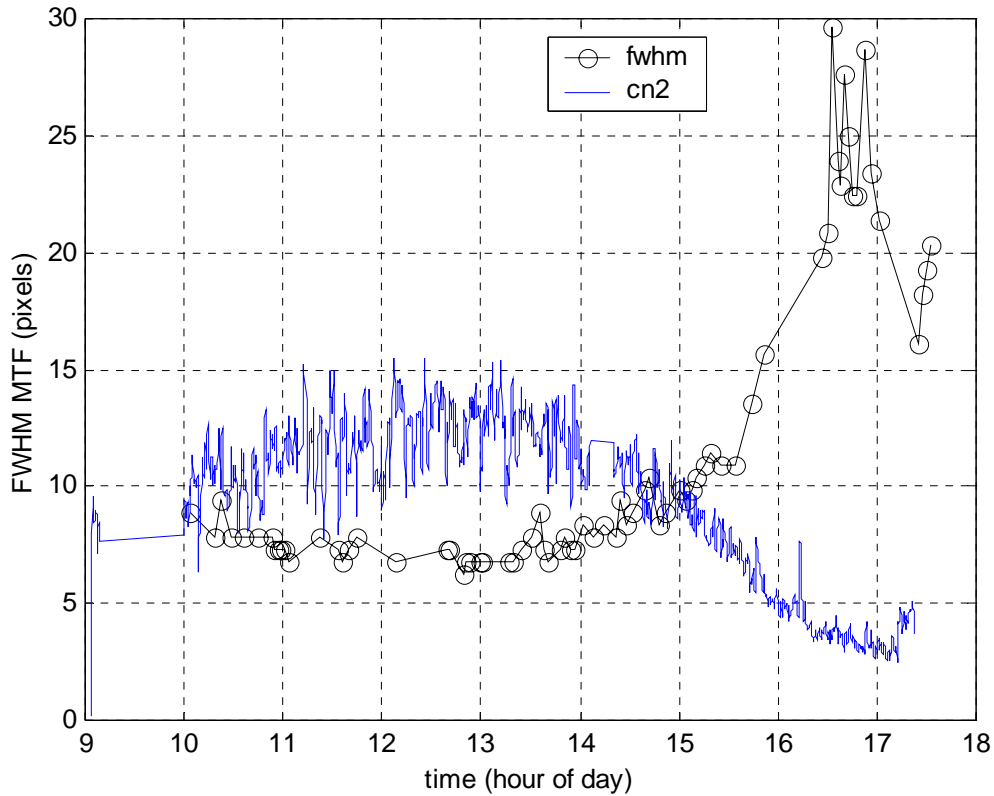

Figure 26. MTF vs. C_n^2

List of Publications

Papers published in non-peer-reviewed journals or in conference proceedings:

M. S. Belen'kii, K. Burgi, P. Gillespie, G. G. Gimmestad, K. Hughes, D. Roberts, J. Stewart, and J. Wood, "Measurement of Tilt Anisoplanatism with Discrete and Extended Sources," SPIE Free-Space Laser Communication and Active Laser Illumination III Conference, Aug. 2003.

Manuscripts submitted but not published:

M. S. Belen'kii, P. Gillespie, G. G. Gimmestad, K. Hughes, V. Rye, D. Roberts, J. Stewart, and J. Wood, "Target Edge Response," SPIE Free-Space Laser Communication and Active Laser Illumination IV Conference, Aug. 2004.

List of Participating Scientific Personnel

Georgia Tech Research Institute
Dr. Gary G. Gimmestad
David W. Roberts
John M. Stewart
Jack W. Wood

Trex Enterprises Corporation
Dr. Mikhail Belen'kii
Kenneth Burgi
Kevin Hughes

Army Research Laboratory
Dr. Patti Gillespie

Report of Inventions

1. Imaging device for remote measurements of wind and optical turbulence parameters

Bibliography

1.   M. S. Belen'kii, S. J. Karis, J. M. Brown, and R. Q. Fugate, "Measurements of tilt angular anisoplanatism," *in Adaptive Optics and Applications*, R. K. Tyson and R. Q. Fugate, eds., Proc. SPIE, Vol. 3126, 481-487(1997).

2.   M. S. Belen'kii, "Tilt angular anisoplanatism and a full–aperture tilt –measurement technique with a laser guide star," Appl. Optics, **39**, 6097-6108(2000).

3.   M. S. Belen'kii, J. M. Stewart, and P. Gillespie, "Turbulence-induced edge image waviness: theory and experiment," Appl. Optics, Vol. 40, 1321-1328(2001).

4.   D. L. Fried, "Varieties of anisoplanatism," in *Imaging through the Atmosphere*, J. C. Wyant, ed. Proc. SPIE, Vol. 75, 20-29(1976).

5.   C. Higgs, H. Barclay, J. Kansky, D. Murphy, and C. A. Primermann, "Adaptive-optics compensation using active illumination," in *Airborne Laser Advanced Technology,* Proc. SPIE, Vol. 3381, 47-56(1998).

6.   M. Belen'kii, T. Brinkley, K. Hughes, and A. Tannebaum, "Tracking through laser-induced clutter for air-to-ground directed energy system," in *Laser System Technology*, Proc. SPIE, Vol. 5087, (2003).

7.   R. Q. Fugate, "Laser beacon adaptive optics for power beaming applications," in *Laser Power Beaming*, SPIE Proc. Vol. 2121, 68-76(1994).

8.   S. D. Ford, D. G. Voelz, V. L. Gamiz, S. L. Storm, S. R. Czyzak, J. Oldenettel, and A. Hanter, "Geo Light Imaging National Testbed (GLINT): past, present, and future," Digital Image recovery and Synthesis IV, T. J. Schulz and P. S. Idell, eds., Proc. SPIE , Vol. 3815, pp2 -10 (1999).

9.   R. Beland, "Propagation through Atmospheric Turbulence," *in Infrared & Electro-Optical Systems Handbook*, Vol. 2 Atmospheric Propagation of Radiation, SPIE pp.153-233, 1993.

10.   V. I. Tatarskii, *Wave Propagation in Random Medium*, (McGraw-Hill, New York, 1960)

11.   A. Consortini, "Role of the inner scale of atmospheric turbulence in optical propagation and method to measure it," in Scattering in Volumes and Surfaces, Ed. M. Nieto-Vesparinas and J. C. Dainty, Elsevier Science Publishers, (North Holland) 1990.

12.   M. S. Belen'kii, S.J. Karis, J. M. Brown II, and R. Q. Fugate, "Experimental validation of a technique to measure tilt from a laser guide star, Opt. Lett,   Vol**.** 24, 637-639(1999).